*energies*

MDPI

*Article*

# Propagation Model for Ground-to-Aircraft Communications in the Terahertz Band with Cloud Impairments

**Vladimir Doborshchuk [1], Vyacheslav Begishev [1,*] and Konstantin Samouylov [1,2]**

[1] Applied Informatics and Probability Theory Department, Peoples' Friendship University of Russia (RUDN University), 117198 Moscow, Russia
[2] Institute of Informatics Problems, Federal Research Center Computer Science and Control of Russian Academy of Sciences, 119333 Moscow, Russia
* Correspondence: begishev-vo@rudn.ru; Tel.: +7-903-559-87-64

**Abstract:** By operating over a large bandwidth, the terahertz (THz) frequency band (0.3–3 THz) promises to deliver extremely high data rates. While the use of this band in cellular communications systems is not expected to happen within the next decade, various other use-cases such as wireless backhauling and point-to-point wireless access are on the immediate horizon. In this study, we develop an analytical propagation model for the case of ground-to-aircraft communications by explicitly accounting for THz-specific propagation phenomena including path loss, attenuation by different types of clouds, and atmospheric absorption at different altitudes. To this aim, we first exhaustively characterize the geometric, molecular, and structural properties of clouds for different weather conditions and Earth regions. Then, by applying the tools of stochastic geometry, we present the closed-form expression for received power at the aircraft. Our numerical results show that the type of weather forming different compositions of clouds provides a major impact on the overall path losses and thus the attained data rates. Specifically, the difference between sunny and rainy conditions may reach 30–50 dB. The overall path loss also heavily depends on the region time and the difference may reach 10–30 dB. The worst conditions are logically provided by rain, where the additional attenuation on top of sunny conditions reaches 50 dB over the whole THz band. The Middle Earth zone is also the worst out of the considered regions with additional attenuation reaching 30 dB. The developed model can be used as a first-order approximation for ground-to-aircraft THz channel modeling.

**Keywords:** Terahertz; propagation model; path loss; ground-to-aircraft; cloud attenuation



**Citation:** Doborshchuk, V.; Begishev, V.; Samouylov, K. Propagation Model for Ground-to-Aircraft Communications in the Terahertz Band with Cloud Impairments. *Energies* **2022**, *15*, 8022. https://doi.org/10.3390/en15218022

Academic Editors: Marian Rusek, Michał Szymański and Dariusz Strzęciwilk

Received: 21 September 2022
Accepted: 25 October 2022
Published: 28 October 2022



## 1. Introduction

The proliferation of new wireless services constantly increases the demand for broadband wireless communications. In response, the data transfer rate over a wireless medium has doubled every eighteen months over the past few decades [1,2]. In recent years, there has been growing interest in wireless communication systems operating in the lower end of the terahertz frequency band (THz, 100–300 GHz) due to their large bandwidth leading to increased throughput [2,3]. Potential applications include data center traffic exchange points, high-definition television (HDTV), terabits for personal and local area networks, cellular networks, vehicular communications, and high-speed backhauls [4,5]. Some of these applications are already supported in IEEE 802.15.3d standard ratified in 2019 [6].

One of the interesting prospective use-cases for THz communications that received attention recently is enabling broadband connectivity with aircraft [7–10]. However, so far most of the attention has been paid to space-to-aircraft communications within the context of 3GPP non-terrestrial networks as higher altitudes are less affected by atmospheric absorption. Specifically, the authors in [7] developed a propagation model by accounting for different altitudes of satellite and aircraft as well as atmospheric absorption. Further,

the authors in [8] analyzed the usage of aircraft as relaying nodes in space–aircraft–ground communications. Direct space-to-ground communications in the THz band are considered in [10]. However, they did not account for propagation specifics of ground-to-aircraft links. Propagation models for different altitudes are proposed in [9]. However, the authors do not account for the attenuation caused by cloud formations. There are also multiple models assessing this type of channel at other frequencies that do not have THz-specifics such as atmospheric absorption and specific cloud attenuation [11,12], and a plethora of papers recently addressed UAV-to-ground channels, see [13].

In this paper, we advocate for ground-to-aircraft communications. The ultimate goal of such a system is Internet access provisioning for passengers and usage of aircraft as relaying points in space–aircraft–ground communications similarly to [10]. The advantages of utilizing ground-mounted stations instead of satellites are much smaller latency and virtually no limitations on complexity and emitted power of ground-mounted communicating units. In order to design such kind of system and to decide upon its operational parameters, a propagation model is required.

Two unique impairments that need to be taken into account when designing the ground-to-aircraft THz propagation models are altitude-dependent atmospheric absorption and attenuation by the clouds. The former component is well-described in literature for fixed altitude and is known to produce exponential attenuation on top of conventional power-law free space losses [14,15]. Cloud impairments are much more difficult to account for due to different types of clouds and their physical and chemical properties [16,17]. Over the past few years, many research groups have focused their efforts on obtaining an extended description of weather effects in the THz band. In particular, the THz attenuation and channel degradation are caused by atmospheric compounds in clouds (particularly, water vapor), airborne particles (such as dust, fog, clouds, and rain), and refractive index in-homogeneity which are caused by air turbulence and related scintillation. However, there are still no studies accounting for these effects in propagation modeling for ground-to-aircraft communications.

The aim of the paper is to develop an analytical propagation model for ground-to-aircraft communications in the THz frequency band. Specifically, by accounting for the specifics of atmospheric absorption as well as cloud impairments, we deliver a closed-form expression for received signal strength at the aircraft. To this aim, we utilize the tools of stochastic geometry by estimating the overall attenuation caused by crossing the clouds at multiple levels. The developed model may serve as a first-order approximation when designing ground-to-aircraft communications systems operating in the THz frequency band.

The main contributions of our study are:

- Detailed overview and classification of the types of clouds, their impairments for THz propagation, and the associated procedure for calculating attenuation induced by a single cloud;
- Analytical propagation model allowing to assess the impairments produced by atmospheric absorption and cloud attenuation in different weather conditions and geographical regions;
- Numerical results showing that the path loss heavily depends on the type of the weather in Earth regions with differences reaching 30–50 and 10–30 dB.

The rest of the paper is organized as follows. First, in Section 2, we concentrate on the characterization of cloud types and their impairments for the THz propagation. In Section 3, we define the system model for the considered ground-to-aircraft communications scenario. Further, in Section 4, we develop the analytical propagation model by accounting for atmospheric absorption and cloud impairments. In Section 5, we present our numerical results and discuss them. Conclusions are provided in the last section.

## 2. Characterization of Cloud Types and Their Impairments

In this section, we first overview the THz propagation properties. Then, we proceed to review the properties of clouds and their impairments on THz propagation. Finally, we demonstrate how to calculate attenuation induced by different types of clouds. The main notation utilized in the paper is presented in Table 1.

**Table 1.** The main notation utilized in this paper.

| Characteristic | Description |
|---|---|
| $\gamma_c$ | Cloud attenuation per kilometer, dB/km |
| $\sigma_e, \sigma_s, \sigma_a$ | Extinction, scattering and absorption coefficients |
| $N(r)$ | Particle size distribution of clouds |
| $K_l$ | Attenuation coefficient, (dB/km)/(g/m$^3$) |
| $\omega$ | Liquid water content, g/m$^3$ |
| $p_w(t)$ | Cloud liquid water density |
| $L$ | Cloud attenuation for particular distance, km |
| $P_{out}(f,d)$ | Received power aircraft antenna, dB |
| $K(f,x)$ | Overall absorption coefficient |
| $L_C(f,d)$ | Clouds overall attenuation, dBm |
| $L_A(f,d)$ | Absorption loss, dBm |
| $p_C$ | Cloud blockage probability |
| $p_k(f,d)$ | Cloud blockage probability on layer k |

### 2.1. THz Propagation Properties and Models

Most THz measurements performed so far focus on indoor short-range scenarios that are limited in terms of propagation distance and usually require perfect synchronization between the transmitter (Tx) and receiver (Rx). The latter is due to the lack of fully functional communications equipment available for frequencies higher than 100 GHz. Specifically, there are very few outdoor measurement campaigns at frequencies above 100 GHz, and they are primarily focused on LoS propagation using either reflected materials or VNA-based extensions of the RF-over-fiber system [18].

While the principal THz-specific propagation effects have been characterized in detail so far [14,19], limited THz channel measurements and models are available for mobile THz systems. These results are scarce and target very specific scenarios, e.g., vehicular-to-vehicular [20,21], train-to-infrastructure [22], indoor [23,24], as well as static use-cases [25]. Specifically, the detailed THz measurements campaign for vehicle-to-vehicle (V2V) communications environment performed in [21] has revealed that the major channel parameters are drastically different from state-of-the-art mmWave measurements at 28, 60, and 72 GHz [26,27], suggesting that the same will hold for THz systems. The human body blockage THz measurements performed in [28] also qualitatively agree with these conclusions. The studies in [29,30] further confirmed these observations with a measurements campaign performed in the office and in microcell environments and proposed a 3GPP-style model fitting the measurement data. Ref. [31] used measurements in an indoor conference room at 140 GHz to develop a mixed ray-tracing and stochastic channel. Several channel models for the THz band were compared and evaluated in [32]. The penetration losses in an office environment have been reported in [33]. In general, the information in studies on outdoor signal propagation in the THz range is sufficient to analyze the influence of water vapor, oxygen, and other atmospheric components.

The impact of atmospheric effects such as rain, fog, snow, and clouds is significantly less studied in the THz band. Specifically, rain attenuation is the most severe effect at frequencies below 90 GHz [34]. At frequencies above 100 GHz, the effects of rain tend

to be constant, while attenuation due to water vapor and clouds becomes more relevant. To improve knowledge of atmospheric propagation at millimeter and THz frequencies, the work should be focused on conducting experimental measurement studies aimed at confirming the validity of existing attenuation models, and further studying the interaction between radiation and the atmosphere, especially in the presence of water particles [35,36]. The most important factor is that it is water particles and liquid crystals in the clouds that will be the catalyst for signal dispersion, and accordingly, under such conditions, power losses will be extremely high.

### *2.2. Classification of the Clouds*

When studying the time-averaged characteristics of clouds, one should keep in mind that they refer only to that part of the period during which cloudiness was observed. Frequencies for general cloud cover, low-level clouds, and vertical extent clouds over continents and oceans can be found in climate guides and atlases. By including the results of aviation soundings, it is further possible to estimate the frequency of cloudiness at the upper and middle levels. For large regions, the total cloud cover and the amount of any type of cloud present can be estimated using satellite measurements. The frequency of cloudiness is closely related to the general circulation of the atmosphere, the nature of the underlying surface, and insolation. In addition, the height of the site, orography, and other factors affect the frequency of cloudiness [37].

According to the World Meteorological Organization (WMO), a cloud is defined as a collection of very small drops of water (above 0 °C), ice crystals (between −20 °C and −40 °C), or their mixture, the presence of which is predominantly observed in the troposphere at different heights above ground level. This organization also gives a generally accepted classification of the various types of clouds. It is worth considering the fact that all clouds have a non-static vertical thickness, and this can vary depending on the particular type of layer and type of cloud. In Table 2, averaged values are provided for most types of clouds.

**Table 2.** Cloud classification in different Earth regions [38,39].

| Cloud Tier | Cloud Type | Lower Boundary Height (km) | Liquid Crystal Density (g/m$^3$) | Vertical Thickness (km) | Temperature (°C) |
|---|---|---|---|---|---|
| High | Pinnate (Ci) | 6–12 | 0.03 | 0.1–1.0 | below −25 |
| | Cirrocumulus (Cc) | 6–12 | 0.03 | 0.3 | |
| | Cirrostratus (Cs) | 6–12 | 0.10 | 0.1–1.0 | |
| Middle | Altocumulus (Ac) | 2–6 | 0.20 | 0.2–0.7 | 0 to −20 |
| | Altostratus (As) | 2–6 | 0.41 | 0.5 | |
| | Nimbostratus (Ns) | Earth—3 | 0.611 | 0.8 | 0 to −25 |
| Lower | Stratocumulus (Sc) | 0.3–1.35 | 0.30 | 0.5 | 0 to −10 |
| | Layered (St) | Earth—0.6 | 0.42 | 0.6 | |
| | Cumulus (Cu) | 0.3–1.5 | 1.00 | 2.0 | |
| | Cumulonimbus (Cb) | 0.6–1.5 | 0.51 | 3.0 | |

The radii $r$ of water particles inside clouds range from 1 μm to approximately 30 μm [39]. A standard value of around 200 μm is also commonly suggested as the limiting liquid particle diameter above which droplets can cause drizzle or rainfall [38]. As for ice crystals, their presence is observed in clouds located in the upper troposphere, which are also known as cirrus clouds. These solid hydrometeors take various forms, including bullets, rosettes, thick plates, short pillars, etc., the maximum dimensions of which vary greatly depending on the type of ice crystal and range from 100 μm to 1500 μm [40].

*2.3. Attenuation by Clouds*

In general, the mechanisms underlying cloud attenuation are those that arise when cloud particles interact with electromagnetic radiation. Specifically, the loss of energy passing through the cloud volume is determined by absorption processes, which are understood as the sum of absorption and scattering effects caused by liquid water drops. These particles can be considered, in essence, as ideal dielectric spheres; thus, Mie's theory of single scattering, widely described in several textbooks such as [41,42], provides the basis for an accurate estimate of the extinction, scattering and absorption coefficients, or the so-called cross sections, $\sigma_e$, $\sigma_s$, and $\sigma_\alpha$, (in square meters), where $\sigma_e = \sigma_s + \sigma_\alpha$. From these parameters, the specific attenuation $\gamma_c$ (in decibels per kilometer) caused by a combination of water spheres with different radii $r$ (in millimeters) is provided by [43]

$$\gamma_c = 4.343 \times 10^3 \int \sigma_e(r) N(r) dr, \tag{1}$$

where $N(r)$ is the particle size distribution of the cloud, and the corresponding product $N(r)dr$ determines the density of water droplets of the cloud with radius $r$. The coefficient $4.343 \times 10^3$ describe the fundamental definitions for the density of a liquid in rain/fog/cloud spheres as specified in [44,45].

The behavior of $N(r)$ for a population of cloud drops usually modeled by a modified gamma function of the form

$$N(r) = ar^\alpha \exp(-br^\beta), \tag{2}$$

where the parameters $a$, $b$, $\alpha$, and $\beta$ are positive real constants.

Note that the use of micro-physical cloud modeling to extract $N(r)$ and calculate cloud attenuation using Mie theory can be simplified using the Rayleigh approximation. The validity of the Rayleigh approximation is taken as the starting point in the Recommendation ITU-R P.840-6 [46] for calculating $\gamma_c$ after extensive propagation studies carried out in the 1980s on absorption by suspended water droplets [47,48]. Using this approximation, the value of $\gamma_c$ is expressed in terms of the liquid crystal content $w$ in the cloud and the specific attenuation coefficient $K_l$, measured as the ratio (dB/km)/(g/m$^3$),

$$\gamma_c = K_l \omega, \tag{3}$$

where $K_l$ is given by

$$K_l = \frac{0.819 f}{\epsilon''(\eta^2 + 1)}, \tag{4}$$

where $f$ is the signal frequency and $\eta = (\epsilon' + 2)/\epsilon''$. The coefficient 0.918 is a part of the empirical approximation from ITU-R P.840.

Curves $K_l$ are shown in Figure 1 for some representative cloud drop temperatures. Here, a seven-year database collected at Adolfo Suárez Madrid–Barajas Airport was used as input for cloud attenuation estimation. The presence of clouds is determined by the Salonen and Uppala model, which is also used to calculate $\omega$. Statistical data in the form of complementary cumulative distribution functions (CCDFs) of zenith cloud attenuation values are shown in Figure 2.

Note that the Rayleigh approximation is most effective between 1 and 1 THz for a temperature range of ±40 °C. To obtain the values of $\epsilon'$ and $\epsilon''$, which are the real and imaginary parts of the permittivity of water, one may utilize the following approximations [45]

$$\begin{aligned} \epsilon'(f) &= \epsilon_2 + \frac{(\epsilon_0 - \epsilon_1)}{1 + (f/f_D)^2} + \frac{(\epsilon_1 - \epsilon_2)}{1 + (f/f_S)^2}, \\ \epsilon''(f) &= \frac{f(\epsilon_0 - \epsilon_1)}{f_D[1 + (f/f_D)^2]} + \frac{f(\epsilon_1 - \epsilon_2)}{f_S[1 + (f/f_S)^2]}, \end{aligned} \tag{5}$$

where $T$ is expressed in Kelvin, and the remaining parameters are: $\phi = 300/T$, $f_D = 20.09 - 142(\phi - 1) + 294(\phi - 1)^2$, $f_S = 590 - 1500(\phi - 1)$, $\epsilon_1 = 5.48$, $\epsilon_2 = 3.51$, $\epsilon_0 = 77.67 + 103.3(\phi - 1)$.

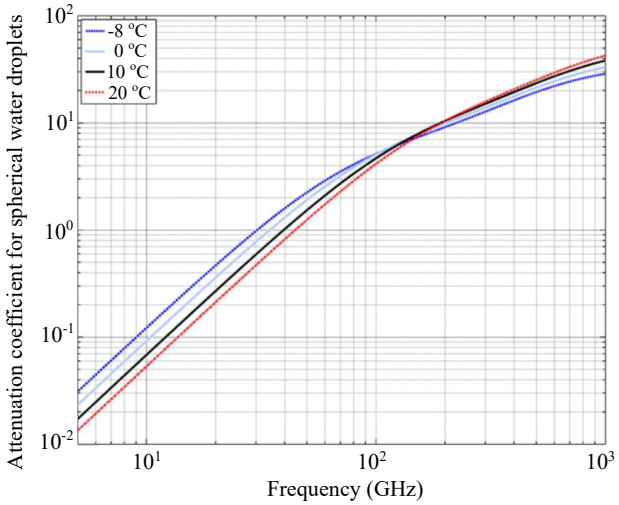


**Figure 1.** Attenuation coefficient for spherical water droplets at several temperatures.

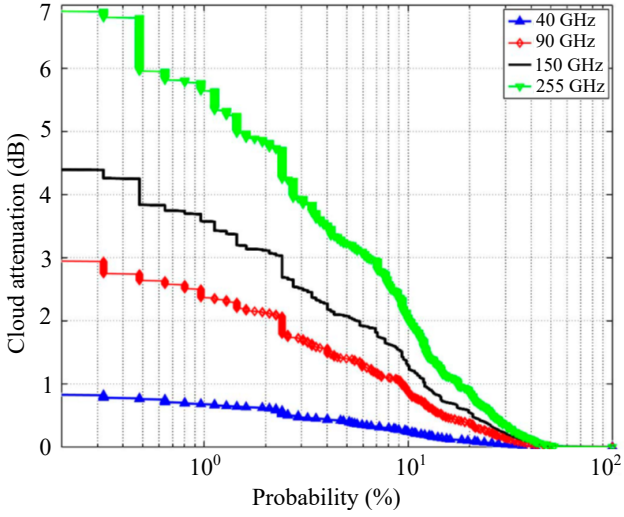


**Figure 2.** Empirical CCDF of zenith cloud attenuation values.

Despite the available values for the density of liquid crystals, it is conventional to utilize approximations for these values. An estimate of the density of liquid crystals $w$ in grams per cubic meter at each cloud layer can be obtained from the air temperature in the layer and its height relative to the lower boundary as [49]

$$w = \begin{cases} w_0(1 + ct)\left(\frac{h_c}{h_r}\right)p_w(t), & t \geq 0\,^{\circ}\mathrm{C}, \\ w_0 e^{ct}\left(\frac{h_c}{h_r}\right)p_w(t), & t < 0\,^{\circ}\mathrm{C}, \end{cases} \tag{6}$$

where $w_0 = 0.17$ (g/m$^3$), $c = 0.04$ ($^{\circ}$C$^{-1}$), $t$ is the temperature in Celsius, $h_r = 1500$ m, $h_c$ is the height from the lower boundary of the layer.

Cloud liquid and water fraction of ice density $p_w(t)$ is approximated as [50]

$$p_w(t) = \begin{cases} 1, t > 0\,^\circ\text{C}, \\ 1 + \frac{t}{20}, -20\,^\circ\text{C} < t \leq 0\,^\circ\text{C}, \\ 0, t \leq -20\,^\circ\text{C} \end{cases} \quad (7)$$

The final attenuation value $L$ is expressed as the product of the specific average attenuation and the distance to a particular cloud layer from the ground in kilometers as

$$L = \gamma_c d_c \quad (8)$$

### *2.4. Clouds Composition in Different Regions*

In order to calculate the overall impairments by clouds, in addition to the provided attenuation assessment, one needs to provide cloud composition in different regions. This is provided in Table 3, showing the prevalence of certain types of clouds in Earth regions [51]. By analyzing the presented data one may observe that the equatorial line is dominated by cloud bands of the intratropical convergence zone (ITC), which are characterized by the convergence of air currents and intense ascending air movements. In this cluster, cumulus and cumulonimbus clouds often develop in combination with a large number of cirrus clouds. Such a cluster is characterized by a multiple components, separated by cloudless gaps, stretching parallel to the equator. Sometimes it is not possible to detect a single cloud band in the ITC region over a distance of a thousand kilometers; in this case, only cloudless areas and small cloud accumulations are observed. In summer and winter, the shapes of the clouds forming the frontal band are the same. Based on this, in sunny weather, almost absolute cloudlessness is observed, while the transition to precipitation occurs immediately, without the presence of cloudy weather.

**Table 3.** The distribution of clouds in different weather conditions and Earth regions.

| **Region** | **Weather** | | |
|---|---|---|---|
| | ***Sunny*** | ***Cloudy*** | ***Rain*** |
| Equator | No clouds | Cumulus (Cu) | Pinnate (Ci)<br>Cirrocumulus (Cc)<br>Cumulonimbus (Cb) |
| Middle zone | Pinnate (Ci)<br>Cumulus (Cu) | Cirrocumulus (Cc)<br>Stratocumulus (Sc)<br>Layered (St)<br>Altocumulus (Ac) | Pinnate (Ci)<br>Cumulonimbus (Cb)<br>Nimbostratus (Ns)<br>Altostratus (As) |
| North | Layered (St) | Stratocumulus (Sc)<br>Layered (St)<br>Altocumulus (Ac) | Stratocumulus (Sc)<br>Layered (St)<br>Cumulus (Cu)<br>Cumulonimbus (Cb) |

In the northern polar regions, stratus and stratocumulus clouds dominate. At the same time, the height of stratus clouds is often below the range from 100 to 200 m. The relative humidity of the lower layers of air in the polar regions (in the Arctic and Antarctic) is close to saturation throughout the year, despite the low absolute humidity. The high frequency of powerful inversions significantly weakens the air exchange, and therefore a significant amount of moisture accumulates under the inversions. The high degree of stability of warmer air masses coming here from adjacent areas is enhanced due to the presence of deep inversions in the polar regions in a layer up to 1.5–2.5 km or more. In winter, inversions occur as a result of radiative air cooling in anticyclones, and in summer as a result of melting snow and ice. All this determines the large horizontal extent of cloud fields, reaching about 1000 km, the long duration of their existence, and the dominance

of stratus clouds. The frequent formation of several inversion layers in the atmosphere causes a high frequency of multilayer clouds. The dominant forms of intramass clouds in the Arctic are stratocumulus and stratus. Cumulus clouds are observed, although rarely, over the coast or archipelagos.

When considering the regions of the middle zone, a temperate climate is often observed, leading to almost equal popularity of ice and mixed clouds. Naturally, pure water clouds most often occur in the warm half of the year, and ice clouds—in the cold half. On a sunny day, the Sun warm the ground, which warms the air directly above it. The heated air, due to convection, rises to the top and forms cumulus clouds. If one looks at a sky filled with cumulus clouds, one can observe that these clouds have a flat bottom, located at the same level for all the clouds. At this altitude, air rising from ground level cools down to the dew point. In summer, cumulonimbus often form cumulonimbus, which can already warn of heavy rains and, accordingly, be accompanied by them. During overcast weather, stratus clouds of various types predominate, but rain is unlikely. Winters are also dominated by high-altitude cirrus clouds, so they can also be a source of precipitation, and they can also accompany the summer period.

## 3. System Model

In our paper, we consider a direct communications link between ground-mounted designated base station (BS) and an aircraft, see Figure 3. Both BS and aircraft are assumed to be equipped with transceivers with perfectly aligned beams. The aircraft of interest is assumed to be an altitude of $d$ km. We consider the system in stationary conditions, where the movement of the aircraft is assumed to produce no additional impairment for communications. Due to the high flying altitude, we neglect the height of BS.

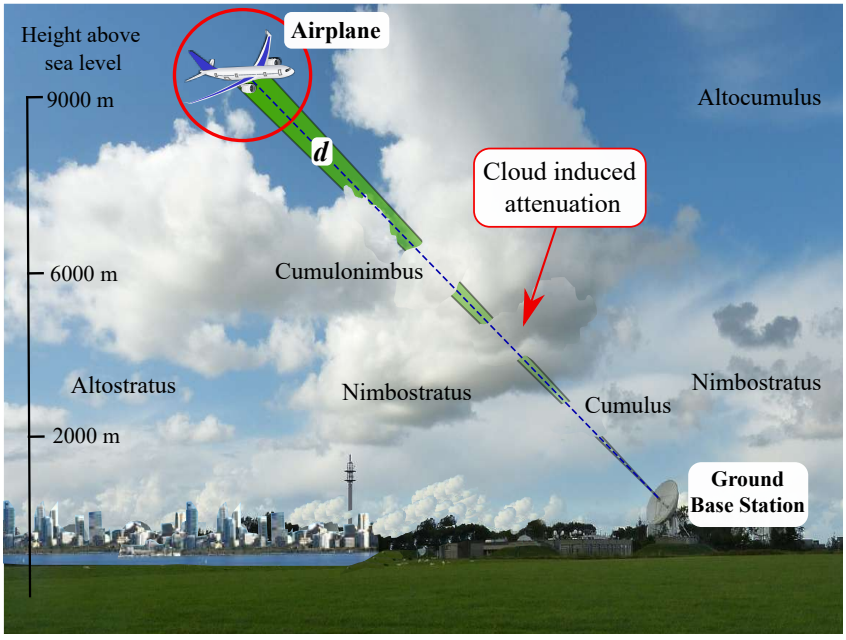


**Figure 3.** A direct communications link between ground-mounted designated BS and an aircraft.

For certainty, we consider uplink transmission from ground BS to aircraft. By accounting for atmospheric absorption by water vapor and oxygen, the received power air aircraft antenna can be expressed as

$$P_{out}(f,d) = P_{in}\left(\frac{4\pi f d}{c}\right)^{-2} \frac{G_R G_T}{L_A(f,d)L_C(f,d)}, \tag{9}$$

where $P_{in}$ is the emitted power at ground BS, $G_T$ and $G_R$ are transmit and receive antenna gains, $L_A(f,d)$ is the attenuation due to absorption in the atmosphere, $L_C(f,d)$ is the

propagation losses due to cloud blockage, $f$ is the carrier frequency, $c$ is the speed of light, and $d$ is the distance between the BS and the aircraft.

The propagation model in (9) features two unknowns, the average attenuation coefficient due to absorption in the atmosphere, $L_A(f,d)$, and the overall losses due to cloud blockage, $L_C(f,d)$. In the next section, we will determine these unknowns.

## 4. Propagation Model

In this section, we parameterize the model by providing first the average attenuation coefficient due to absorption in the atmosphere, $L_A(f,d)$, and then the overall losses due to cloud blockage, $L_C(f,d)$.

### *4.1. Atmospheric Absorption*

To determine $\alpha_e$, one needs to calculate absorption loss $L_A(f,d)$ that depends on the distance between ground BS and aircraft $d$. According to [14,15], it is defined as

$$L_A(f,d) = \frac{1}{\tau(f,d)}, \tag{10}$$

where $\tau(f,d)$ is the transmittance of the medium following the Beer–Lambert law, $\tau(f,d) \approx e^{-K(f,x)}$, $K(f,x)$ is the overall absorption coefficient of the medium at the altitude $x$.

The frequency- and altitude-dependent absorption coefficient $K(f,x)$ can be represented as [14]

$$K(f,x) = \sum_{i,g} k^{i,g}(f,x), \tag{11}$$

where $k^{i,g}(f,x)$ represents the individual absorption coefficient for the isotopologue $i$ of gas $g$ at altitude $x$. The coefficients $k^{i,g}(f,x)$ are available from the HITRAN database [52]. Finally, the average attenuation coefficient due to absorption in the atmosphere is provided by integration,

$$L_A(f,d) = \int_0^d \sum_{i,g} k^{i,g}(f,x)dx. \tag{12}$$

### *4.2. Blockage by Clouds*

The next component to determine is the attenuation by the cloud $L_C(f,d)$. Recall that the attenuation caused by a single layer of clouds has been calculated in Section 2. However, depending on weather conditions, a propagation path may or may not be occluded by a cloud at each layer. Thus, the overall attenuation caused by clouds can be approximated by

$$L_C(f,d) = E\left[\sum_{k=1}^{K} p_k L_k\right], \tag{13}$$

where $p_k$ is the probability that clouds at layer $k$ occludes the propagation path, $L_k$ is attenuation induced by cloud blockage at layer $k$ computed in Section 2. We now proceed with deriving $p_k$ by using the tools of integral geometry.

Observe that, to determine $p_k$ in (13), we basically need to determine the probability that a point randomly dropped on the plane in $\Re^2$ and representing the intersection of the propagation path and clouds at layer $k$ crosses the cloud and actually induced attenuation in (13). This task can naturally be solved using integral geometry [53] as recently demonstrated in applied studies [38,54]. To proceed, we need two definitions.

**Definition 1** (**Kinematic density**). *Let K be the group of motions of the set A in the plane. The kinematic density of the set of points K is calculated as*

$$dA = dx \cap dy \cap d\phi, \tag{14}$$

*which must be invariant under the group of motions of the plane.*

**Definition 2** (**Kinematic measure**). *The kinematic measure m of a set of group motions K on the plane is defined as the integral of the kinematic density dA over K, i.e.,*

$$m_A = \int_K dA = \int_K dx \cap dy \cap d\phi. \tag{15}$$

Consider one THz BS located in the region $A$ of interest, and let $B$ denote the cloud in this zone, see Figure 4, where multiple clouds $B_i$ shown. First, we are interested in the probability $p_C$ that a ground-to-aircraft transmission path crossing this cloud layer at a randomly chosen point $P$ in $A$ actually crosses the cloud, i.e., $P$ is in $B$. Using the definition of conditional probability, we have

$$p_C = \frac{Pr\{P \in A \cap B\}}{Pr\{A \cap B \neq 0\}}, \tag{16}$$

where the probability that a ground-to-aircraft transmission path crossing this cloud layer at a randomly chosen point $P$ belongs to the intersection of two sets, $A$ and $B$, is in the numerator, and the probability that these sets intersect is in the denominator.

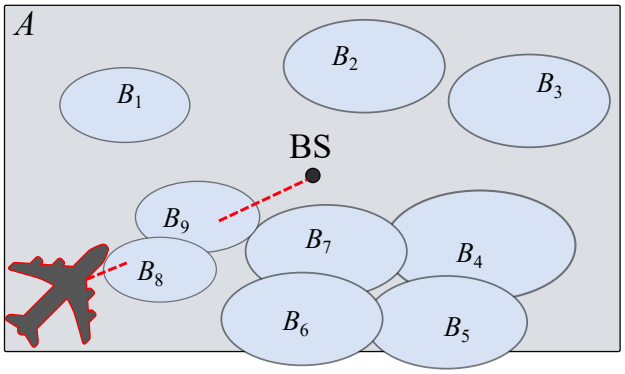


**Figure 4.** Illustration of cloud blockage at a certain cloud layer.

Using the definition of a kinematic measure, we obtain

$$\begin{aligned} Pr\{P \in A \cap B\} &= m(A : P \in A \cap B), \\ Pr\{A \cap B \neq 0\} &= m(A : A \cap B \neq 0), \end{aligned} \tag{17}$$

where the first expression is the kinematic measure of the set of motions $A$ such that $P \in A$, and the second gives the measure of all motions $A$ for which the intersection between $A$ and $B$ is not equal to zero.

Following further calculations from [53], the measures will be equal to

$$\begin{aligned} m_j\{P \in A \cap B\} &= \int_{P \in B} f(x,y) dx \cap dy \cap d\phi, \\ m_j\{A \cap B \neq 0\} &= \int_{A \cap B \neq 0} f(x,y) dx \cap dy \cap d\phi, \end{aligned} \tag{18}$$

where $f(x,y)$ is the distribution of the point $P$ in the set $A$.

Finally, the implied probability is defined as

$$p_C = \frac{\int_{P\in B} f(x,y)dx \cap dy \cap d\phi}{\int_{A\cap B\neq 0} f(x,y)dx \cap dy \cap d\phi}, \tag{19}$$

and can be computed for a particular shape of $A$, $B$ and $f(x,y)$.

The numerator can be calculated as

$$\begin{aligned} m_j\{P \in A \cap B\} &= \int_{P\in B} dx \cap dy \cap d\phi = \\ &= \int_{P\in B} dx \cap dy \int_{P\in B}^{2\pi} d\phi = 2\pi E[S_B], \end{aligned} \tag{20}$$

where $E[S_B]$ is the average area of a cloud.

The measure of motions $A$ at $A \cap B \neq 0$ is expressed as

$$\begin{aligned} m_j\{A \cap B \neq 0\} &= \int_{A\cap B\neq 0} dx \cap dy \cap d\phi = \\ &= 2\pi(S_A + E[S_B]) + L_A E[L_B], \end{aligned} \tag{21}$$

where $E[L_B]$ is the perimeter of a cloud, $S_A$ and $L_A$ are the area and perimeter of $A$.

Substituting (17)–(19), we obtain

$$p_C = \frac{2[S_B]}{2\pi(S_A + E[S_B]) + L_A E[L_B]}. \tag{22}$$

Consider now $\mu_k$ to be the density of clouds at layer $k$ expressed in number of clouds be squared kilometer. Using the results above, the probability that a cloud at layer $k$ occludes the propagation path $p_K$ is given by

$$p_k = 1 - (1 - p_C)^{\lceil \mu_k / S_A \rceil}, \tag{23}$$

where $\lceil \cdot \rceil$ is the rounding operator.

### *4.3. Overall Path Loss*

By utilizing (23) we can complete the parametrization of the model. Observe that the number of cloud layers blocking the propagation path follows multinomial distribution making calculation of the mean cloud impairments in the right-hand side of (13) a complex procedure. Instead, one may utilize the direct approach involving probability generating function (PGF) as follows.

Let $G_{L_C(f,d)}(z)$ denote PGF of the overall cloud impairments, that is,

$$G_{L_C(f,d)}(z) = E\left[z^{L_C(f,d)}\right] = E\left[z^{\sum_{k=1}^{K} I_k L_k}\right], \tag{24}$$

where $I_k$ is the indicator function.

Since the probability of ground-to-aircraft path blockage at layer $i$ is independent from blockage at layer $j$ and the impairment at each layer is assumed to be constant, we can write

$$G_{L_C(f,d)}(z) = G_{I_1}(z^{L_1}) G_{I_2}(z^{L_2}) \times \cdots \times G_{I_N}(z^{L_N}), \tag{25}$$

where $N$ is the overall number of cloud layers, $G_{I_k}(z^{L_k})$ is the PGF of Bernoulli distribution characterizing the impairment at layer $k$. the latter is known to be

$$G_{I_i}(z) = p_k z + (1 - p_k). \tag{26}$$

The use of (24)–(26) allows for simple calculation of (13).

## 5. Numerical Results

In this section, we elaborate on our numerical results. We consider several typical scenarios for weather conditions: (i) cloudless or slightly cloudy, sunny conditions, (ii) cloudy conditions, and (iii) rainy conditions. We also consider different Earth regions. To create a sample set of clouds corresponding to a specific selected region, we use computer simulations with parameters detailed in Section 2. The dimensions of zone $A$ are chosen to be $10^4 \times 10^4$ m. To calculate cloud temperatures, we use uniform distribution over the appropriate interval for a particular type of cloud. In the same way, we approach the formation of the height of a particular cloud and its presence in general, focusing on the currently selected scenario. In the case of clouds whose temperature is lower than $-2$ °C, we utilize tabular values for the content of liquid crystals. The default system parameters are summarized in Table 4.

**Table 4.** The default system parameters.

| Characteristic | Value | Description |
|---|---|---|
| f | 0.1–10 THz | Carrier frequency |
| $d$ | 7000–14,000 m | Ground-to-aircraft distance |
| $P_T$ | 10–200 W | Transmit power |
| $G_T$ | 20–80 dB | Transmit antenna gain |
| $G_R$ | 20–40 dB | Receive antenna gain |
| $S_T$ | 0 dB | SNR outage threshold |
| $N_0$ | $-174$ dBm/Hz | Thermal noise |

Note that the impact of temperature is mainly attributed to both the atmospheric attenuation coefficient and typical clouds for different times of the year. It has to be accounted for in both estimations of the absorption coefficient in Section 4.1 by utilizing appropriated tabulated data from the HITRAN database and when deciding upon the cloud formations. In our numerical results, we consider the year-averaged temperature for different considered Earth regions (north, middle, and equator). As an example of the middle zone, Germany was considered with a year-averaged temperature at the sea level of 8.7 °C, while for the equator, we considered Kenya with the year-averaged value of 29.1 °C. For the north region, we considered Finland with the corresponding value of 5.0 °C. Note that, as the altitude increases, the difference between regions gets smaller. Thus, the overall differences caused by different atmospheric attenuation are negligibly lying within 1–2 dB. However, the formations of clouds also vary depending on the time of the year in different Earth regions. We considered those typical for the summertime. In general, when applying it, one needs to fine-tune the model with the appropriate choice of environmental parameters.

We start by demonstrating the difference between the proposed model accounting for both atmospheric absorption and attenuation by clouds and the standard free-space propagation model (FSPL) in Figure 5. Here, we consider the middle Earth zone and two cloud conditions—rainy and cloudy weather. As one may observe, the difference between the proposed model for rainy conditions and FSPL is 10 dB. For cloudy conditions, it reaches 12 dB. These observations confirm that for accurate aircraft-to-ground THz channel modeling, one needs to account for the impairments considered in this paper.

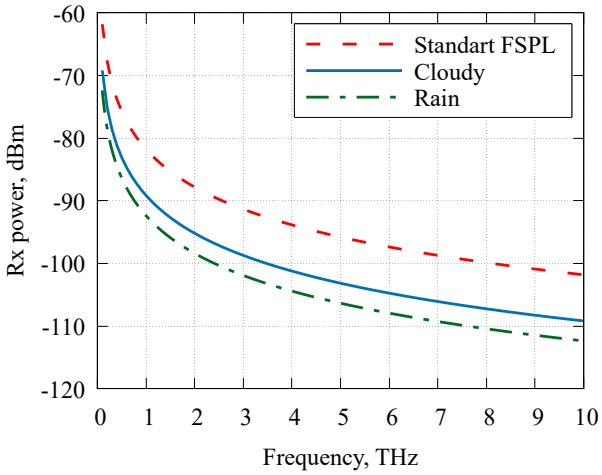


**Figure 5.** The difference between the proposed model accounting for both atmospheric absorption and attenuation by clouds and the standard free-space propagation model.

We proceed by illustrating the utilization of the proposed model for different weather conditions, sunny, cloudy, and rainy in the equator Earth zone in Figure 6. Specifically, Figure 6a,b show Rx power as a function of frequency and aircraft altitude. As one may observe in Figure 6a, logically, sunny conditions produce the best propagation environment across the whole THz band. The difference between sunny and cloudy conditions is approximately 15–20 dB and slightly increases as the carrier frequency increases. Note that these differences are solely attributed to the blockage by clouds and atmospheric absorption as no additional weather effects are present. Further, the difference between cloudy and rainy conditions is around 30–50 dB depending on the frequency and altitude. Here, the additional attenuation is mainly due to both rain and blockage by clouds specific to rainy weather conditions.

By analyzing the presented data further, one may observe that the aircraft altitude, expectedly, provides a linear impact on the Rx power. Similar observations are provided in Figure 6c,e . In general, as one may observe, rainy conditions produces the worst propagation environment for ground-to-aircraft communications in the THz frequency band.

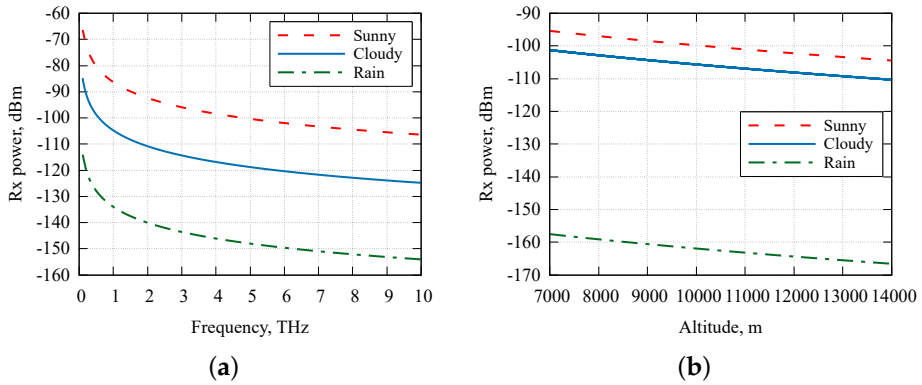


**Figure 6.** *Cont.*

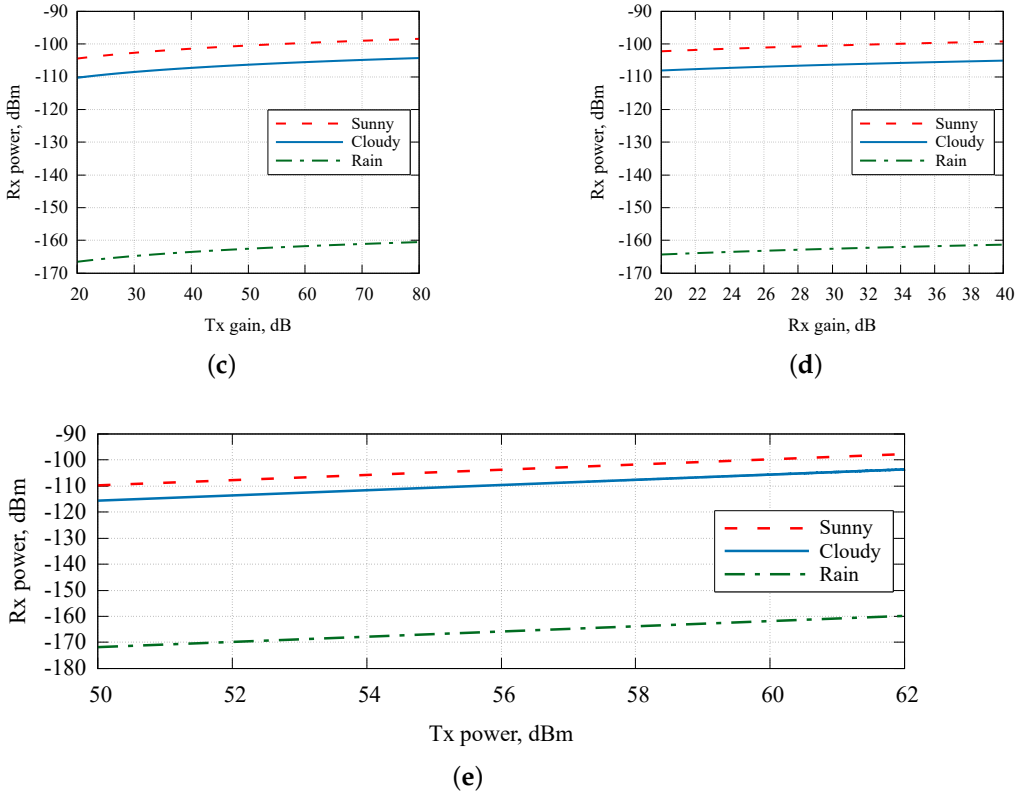


**Figure 6.** The received power in the equator Earth zone. (**a**) Rx power as a function of frequency; (**b**) Rx power as a function of altitude; (**c**) Rx power as a function of Tx gain; (**d**) Rx power as a function of Rx gain; (**e**) Rx power as a function of Tx power.

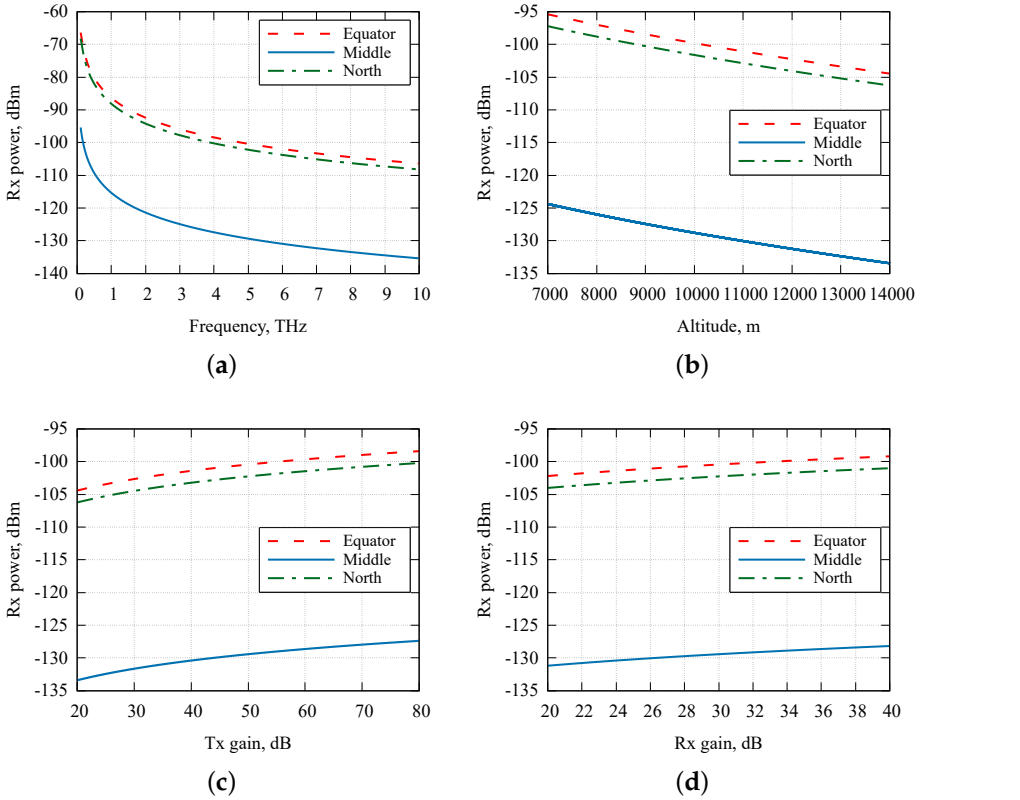


**Figure 7.** *Cont.*

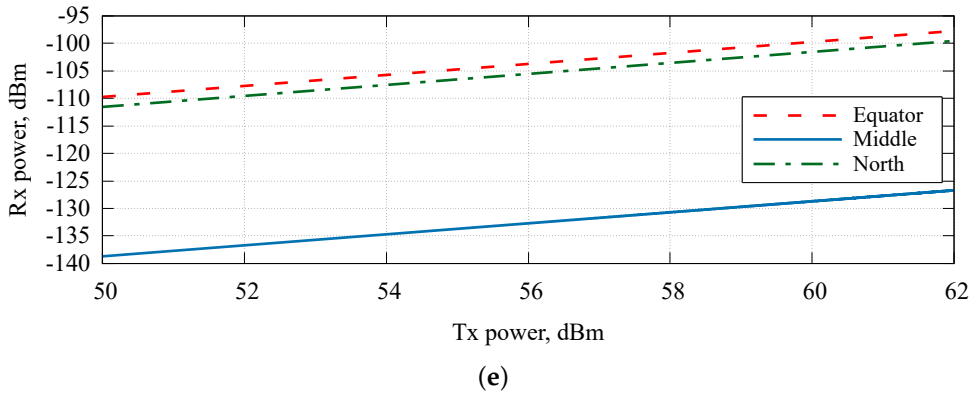


(**e**)

**Figure 7.** The received power in the sunny weather conditions. (**a**) Rx power as a function of frequency; (**b**) Rx power as a function of altitude; (**c**) Rx power as a function of Tx gain; (**d**) Rx power as a function of Rx gain; (**e**) Rx power as a function of Tx power.

We now proceed to assess the effect of different Earth zones, north, equator, and middle part, all in sunny conditions, illustrated in Figure 7. Recall that in these conditions, there are almost no clouds in the equator and north zones, while the impact of clouds in the middle zone is rather limited. This is reflected in the presented illustrations, where the equator is characterized by the best possible propagation conditions. However, the north zone is just 1–3 dB lower in terms of overall impairments. The middle zone, on the other hand, is characterized by much worse conditions, with an additional 15–20 dB of attenuation. These impairments are mainly caused by cloud blockage. We also note that the path loss represented in Figures 6e and 7e is independent of the Tx power and these figures represent the required sensitivity level of Rx needed to receive the data correctly.

## 6. Conclusions

Motivated by the need for enabling high-speed connectivity for aircraft, in this paper, we developed a ground-to-aircraft propagation model for the THz frequency band by accounting for atmospheric absorption and cloud impairments. To this aim, we first studied the geometric and molecular properties of clouds at different layers characterizing their attenuation impairments and composition properties depending on the type of weather conditions and Earth region. Then, we utilized the tools of integral geometry and probability theory to calculate cloud blockage probabilities and characterize the overall cloud-induced attenuation.

In our numerical results, we illustrated the attenuation caused by different weather conditions in different parts of the Earth. Specifically, we have shown that the difference between sunny and rainy conditions may reach 30–50 dB that may require a considerable increase in the emitted power. Secondly, the overall path loss heavily depends on the region time and the difference may reach 10–30 dB. The worst conditions are logically provided by rain, where the additional attenuation on top of sunny conditions reaches 50 dB over the whole THz band. The Middle Earth zone is also the worst out of the considered regions with additional attenuation reaching 30 dB.

The main contribution of the paper is a way to capture cloud-induced attenuation. The proposed model can be utilized as a propagation model when assessing the averaged received signal strength at the aircraft-to-ground links or as a building block for specifying more precise models that involve additional propagation effects such as fading.

**Author Contributions:** Conceptualization, V.B. and K.S.; methodology, V.D.; software, V.B. and V.D.; validation, V.B. and K.S.; formal analysis, V.B.; investigation, V.D.; resources, V.B. and V.D.; data curation, V.B.; writing—original draft preparation, V.B. and K.S.; writing—review and editing, V.D.; visualization, V.B.; supervision, K.S.; project administration, V.B. and K.S.; funding acquisition, K.S. All authors have read and agreed to the published version of the manuscript.

**Funding:** Sections 3–5 were written by Vyacheslav Begishev under the support of the Russian Science Foundation, project no. 21-79-10139. This paper has been supported by the RUDN University Strategic Academic Leadership Program (recipient Konstantin Samouylov, Sections 1, 2 and 6).

**Institutional Review Board Statement:** Not applicable.

**Informed Consent Statement:** Not applicable.

**Data Availability Statement:** Not applicable.

**Conflicts of Interest:** The authors declare no conflict of interest.

## References

1. Schneider, T. Ultrahigh-Bitrate Wireless Data Communications via THz-Links; Possibilities and Challenges. *J. Infrared, Millim. Terahertz Waves* **2015**, *36*, 159–179. [CrossRef]
2. Seeds, A.J.; Shams, H.; Fice, M.J.; Renaud, C.C. TeraHertz Photonics for Wireless Communications. *J. Light. Technol.* **2015**, *33*, 579–587. [CrossRef]
3. Federici, J.F.; Ma, J.; Moeller, L. Review of weather impact on outdoor terahertz wireless communication links. *Nano Commun. Netw.* **2016**, *10*, 13–26. Terahertz Communications. [CrossRef]
4. Petrov, V.; Pyattaev, A.; Moltchanov, D.; Koucheryavy, Y. Terahertz band communications: Applications, research challenges, and standardization activities. In Proceedings of the 2016 8th International Congress on Ultra Modern Telecommunications and Control Systems and Workshops (ICUMT), Lisbon, Portugal, 18–20 October 2016; pp. 183–190.
5. Petrov, V.; Kokkoniemi, J.; Moltchanov, D.; Lehtomäki, J.; Juntti, M.; Koucheryavy, Y. The impact of interference from the side lanes on mmWave/THz band V2V communication systems with directional antennas. *IEEE Trans. Veh. Technol.* **2018**, *67*, 5028–5041. [CrossRef]
6. Petrov, V.; Kurner, T.; Hosako, I. IEEE 802.15. 3d: First standardization efforts for sub-terahertz band communications toward 6G. *IEEE Commun. Mag.* **2020**, *58*, 28–33. [CrossRef]
7. Kokkoniemi, J.; Jornet, J.M.; Petrov, V.; Koucheryavy, Y.; Juntti, M. Channel modeling and performance analysis of airplane-satellite terahertz band communications. *IEEE Trans. Veh. Technol.* **2021**, *70*, 2047–2061. [CrossRef]
8. Liao, A.; Gao, Z.; Wang, D.; Wang, H.; Yin, H.; Ng, D.W.K.; Alouini, M.S. Terahertz ultra-massive MIMO-based aeronautical communications in space-air-ground integrated networks. *IEEE J. Sel. Areas Commun.* **2021**, *39*, 1741–1767. [CrossRef]
9. Saeed, A.; Gurbuz, O.; Akkas, M.A. Terahertz communications at various atmospheric altitudes. *Phys. Commun.* **2020**, *41*, 101113.
10. Suen, J.Y.; Fang, M.T.; Denny, S.P.; Lubin, P.M. Modeling of terabit geostationary terahertz satellite links from globally dry locations. *IEEE Trans. Terahertz Sci. Technol.* **2015**, *5*, 299–313. [CrossRef]
11. Mirza, M.Y.M.; Khan, N.M. G2A Communication Channel Modeling and Characterization Using Confocal Prolates. *Wirel. Pers. Commun.* **2020**, *115*, 745–787. [CrossRef]
12. Mirza, M.Y.M.; Khan, N.M.; Jamal, A.; Ramer, R. Characterization of spatial reflection co-efficient for ground-to-aircraft and satellite-to-aircraft communication. *Appl. Comput. Electromagn. Soc. J. ACES* **2018**, *33*, 56–68.
13. Khawaja, W.; Guvenc, I.; Matolak, D.W.; Fiebig, U.C.; Schneckenburger, N. A survey of air-to-ground propagation channel modeling for unmanned aerial vehicles. *IEEE Commun. Surv. Tutor.* **2019**, *21*, 2361–2391. [CrossRef]
14. Jornet, J.M.; Akyildiz, I.F. Channel modeling and capacity analysis for electromagnetic wireless nanonetworks in the terahertz band. *IEEE Trans. Wirel. Commun.* **2011**, *10*, 3211–3221. [CrossRef]
15. Boronin, P.; Petrov, V.; Moltchanov, D.; Koucheryavy, Y.; Jornet, J.M. Capacity and throughput analysis of nanoscale machine communication through transparency windows in the terahertz band. *Nano Commun. Netw.* **2014**, *5*, 72–82. [CrossRef]
16. Aha, D.W.; Bankert, R.L. Feature selection for case-based classification of cloud types: An empirical comparison. In Proceedings of the AAAI-94 workshop on Case-Based Reasoning, Seattle, WA, USA, 31 July–4 August 1994; Volume 106, p. 112.
17. Nagatsuma, T.; Carpintero, G. Recent Progress and Future Prospect of Photonics-Enabled Terahertz Communications Research. *IEICE Trans. Electron.* **2015**, *E98.C*, 1060–1070. [CrossRef]
18. Xing, Y.; Rappaport, T.S. Propagation Measurements and Path Loss Models for sub-THz in Urban Microcells. In Proceedings of the ICC 2021—IEEE International Conference on Communications, Online, 14–23 June 2021; pp. 1–6. [CrossRef]
19. Han, C.; Bicen, A.O.; Akyildiz, I. Multi-Ray Channel Modeling and Wideband Characterization for Wireless Communications in the Terahertz Band. *IEEE Trans. Wirel. Commun.* **2015**, *14*, 2402–2412. [CrossRef]
20. Petrov, V.; Eckhardt, J.M.; Moltchanov, D.; Koucheryavy, Y.; Kurner, T. Measurements of reflection and penetration losses in low terahertz band vehicular communications. In Proceedings of the 2020 14th European Conference on Antennas and Propagation (EuCAP), Copenhagen, Denmark, 15–20 March 2020; pp. 1–5.
21. Eckhardt, J.M.; Petrov, V.; Moltchanov, D.; Koucheryavy, Y.; Kürner, T. Channel measurements and modeling for Low-Terahertz band vehicular communications. *IEEE J. Sel. Areas Commun.* **2021**, *39*, 1590–1603. [CrossRef]
22. Guan, K.; Peng, B.; He, D.; Eckhardt, J.M.; Rey, S.; Ai, B.; Zhong, Z.; Kürner, T. Measurement, simulation, and characterization of train-to-infrastructure inside-station channel at the terahertz band. *IEEE Trans. Terahertz Sci. Technol.* **2019**, *9*, 291–306. [CrossRef]

23. Kokkoniemi, J.; Petrov, V.; Moltchanov, D.; Lehtomäki, J.; Koucheryavy, Y.; Juntti, M. Wideband terahertz band reflection and diffuse scattering measurements for beyond 5G indoor wireless networks. In Proceedings of the European Wireless 2016; 22th European Wireless Conference, Dresden, Germany, 19–21 September 2016; pp. 1–6.
24. Petrov, V.; Kokkoniemi, J.; Moltchanov, D.; Lehtomaki, J.; Koucheryavy, Y.; Juntti, M. Last meter indoor terahertz wireless access: Performance insights and implementation roadmap. *IEEE Commun. Mag.* **2018**, *56*, 158–165. [CrossRef]
25. He, D.; Guan, K.; Fricke, A.; Ai, B.; He, R.; Zhong, Z.; Kasamatsu, A.; Hosako, I.; Kürner, T. Stochastic channel modeling for kiosk applications in the terahertz band. *IEEE Trans. Terahertz Sci. Technol.* **2017**, *7*, 502–513. [CrossRef]
26. Boban, M.; Dupleich, D.; Iqbal, N.; Luo, J.; Schneider, C.; Müller, R.; Yu, Z.; Steer, D.; Jämsä, T.; Li, J.; et al. Multi-band vehicle-to-vehicle channel characterization in the presence of vehicle blockage. *IEEE Access* **2019**, *7*, 9724–9735. [CrossRef]
27. He, R.; Schneider, C.; Ai, B.; Wang, G.; Zhong, Z.; Dupleich, D.A.; Thomae, R.S.; Boban, M.; Luo, J.; Zhang, Y. Propagation channels of 5G millimeter-wave vehicle-to-vehicle communications: Recent advances and future challenges. *IEEE Veh. Technol. Mag.* **2019**, *15*, 16–26. [CrossRef]
28. Bilgin, B.A.; Ramezani, H.; Akan, O.B. Human blockage model for indoor terahertz band communication. In Proceedings of the 2019 IEEE International Conference on Communications Workshops (ICC Workshops), Shanghai, China, 20–24 May 2019; pp. 1–6.
29. Xing, Y.; Rappaport, T.S.; Ghosh, A. Millimeter wave and sub-THz indoor radio propagation channel measurements, models, and comparisons in an office environment. *IEEE Commun. Lett.* **2021**, *25*, 3151–3155. [CrossRef]
30. Xing, Y.; Rappaport, T.S. Propagation Measurements and Path Loss Models for sub-THz in Urban Microcells. *arXiv* **2021**. arXiv:2103.01151.
31. Chen, Y.; Li, Y.; Han, C.; Yu, Z.; Wang, G. Channel Measurement and Ray-Tracing-Statistical Hybrid Modeling for Low-Terahertz Indoor Communications. *IEEE Trans. Wirel. Commun.* **2021**, *20*, 8163–8176. [CrossRef]
32. Gargari, A.A.; Polese, M.; Zorzi, M. Full-Stack Comparison of Channel Models for Networks above 100 GHz in an Indoor Scenario. In Proceedings of the 5th ACM Workshop on Millimeter-Wave and Terahertz Networks and Sensing Systems. Association for Computing Machinery, 2021, mmNets '21, New York, NY, USA, 25–29 October 2021; pp. 43–48. [CrossRef]
33. Du, K.; Ozdemir, O.; Erden, F.; Guvenc, I. Sub-Terahertz and mmWave Penetration Loss Measurements for Indoor Environments. *arXiv* **2021**. arXiv:2103.02745.
34. Renaud, D.L.; Federici, J.F. Terahertz Attenuation in Snow and Sleet. *J. Infrared* **2019**, *40*, 868–877. [CrossRef]
35. Balal, Y.; Pinhasi, Y. Atmospheric Effects on Millimeter and Sub-millimeter (THz) Satellite Communication Paths. *J. Infrared* **2019**, *40*, 219–230. [CrossRef]
36. Shawon, M.E.; Chowdhury, M.Z.; Hossen, M.B.; Ahmed, M.F.; Jang, Y.M. Rain Attenuation Characterization for 6G Terahertz Wireless Communication. In Proceedings of the 2021 International Conference on Artificial Intelligence in Information and Communication (ICAIIC), Jeju Island, Korea, 20–23 April 2021; pp. 416–420. [CrossRef]
37. Feigelson, E.M. *Radiation in a Cloudy Atmosphere*; Springer Science & Business Media: Berlin/Heidelberg, Germany, 2013; Volume 6.
38. Petrov, V.; Moltchanov, D.; Kustarev, P.; Jornet, J.M.; Koucheryavy, Y. On the use of integral geometry for interference modeling and analysis in wireless networks. *IEEE Commun. Lett.* **2016**, *20*, 2530–2533.
39. World Meteorological Organization. *Guide to Meteorological Instruments and Methods of Observation*; World Meteorological Organization: Geneva, Switzerland, 1996.
40. Brussaard, G.; Watson, P.A. *Atmospheric Modelling and Millimetre Wave Propagation*; Springer Science & Business Media: Berlin/Heidelberg, Germany, 1994.
41. Dissanayake, A.; Allnutt, J.; Haidara, F. Cloud attenuation modelling for SHF and EHF applications. *Int. J. Satell. Commun.* **2001**, *19*, 335–345. [CrossRef]
42. Hulst, H.C.; van de Hulst, H.C. *Light Scattering by Small Particles*; Courier Corporation: Chelmsford, UK, 1981.
43. Pruppacher, H.R.; Klett, J.D.; Wang, P.K. *Microphysics of Clouds and Precipitation*; Taylor & Francis: Hoboken, NJ, USA, 1998.
44. Ulaby, F.T.; Moore, R.K.; Fung, A.K. Microwave Remote Sensing: Active and Passive. Volume 1-Microwave Remote Sensing Fundamentals and Radiometry; NTRS: Washington, DC, USA, 1981.
45. Siles, G.A.; Riera, J.M.; Garcia-del Pino, P. Atmospheric attenuation in wireless communication systems at millimeter and THz frequencies [wireless corner]. *IEEE Antennas Propag. Mag.* **2015**, *57*, 48–61. [CrossRef]
46. ITU-R . Attenuation due to Clouds and Fog. In *ITU-R Recommendation P.840-6*; ITU-R: Geneva, Switzerland, 2013.
47. Ishimaru, A. *Wave Propagation and Scattering in Random Media*; Academic Press: New York, NY, USA, 1978; Volume 2.
48. Liebe, H.J. An updated model for millimeter wave propagation in moist air. *Radio Sci.* **1985**, *20*, 1069–1089. [CrossRef]
49. Luini, L.; Capsoni, C. Efficient calculation of cloud attenuation for earth–space applications. *IEEE Antennas Wirel. Propag. Lett.* **2014**, *13*, 1136–1139. [CrossRef]
50. Luini, L.; Riva, C.; Capsoni, C.; Martellucci, A. Attenuation in nonrainy conditions at millimeter wavelengths: Assessment of a procedure. *IEEE Trans. Geosci. Remote Sens.* **2007**, *45*, 2150–2157. [CrossRef]
51. Martellucci, A.; Baptista, J.P.; Blarzino, G. New climatological databases for ice depolarization on satellite radio links. In Proceedings of the COST 280 1st International Workshop on Propagation Impairment Mitigation for Millimetre Wave Radio Systems, Malvern, UK, 1–3 July 2002.
52. Rothman, L.S. *High-Resolution Transmission Molecular Absorption Database*; Harvard-Smithson Center for Astrophysics: Cambridge, MA, USA, 2014. Available online: www.cfa.harvard.edu (accessed on 15 August 2022).

53. Sors, L.A.S.; Santaló, L.A. *Integral Geometry and Geometric Probability*; Cambridge University Press: Cambridge, MA, USA, 2004.
54. Begishev, V.; Moltchanov, D.; Gaidamaka, A.; Samouylov, K. Closed-Form UAV LoS Blockage Probability in Mixed Ground-and Rooftop-Mounted Urban mmWave NR Deployments. *Sensors* **2022**, *22*, 977. [CrossRef]